J|A|C|S ARTICLES

Published on Web 01/11/2010

Three-Dimensional Chemical Profile Manipulation Using Two-Dimensional Autonomous Microfluidic Control

YongTae Kim,[†] Kerem Pekkan,[†,‡] William C. Messner,*[,†] and Philip R. LeDuc*[,†,‡,§]

Departments of Mechanical Engineering, Biomedical Engineering, and Biological Sciences, Carnegie Mellon University, 5000 Forbes Avenue, Pittsburgh, Pennsylvania 15213-3890

Received September 22, 2009; E-mail: prleduc@cmu.edu; bmessner@andrew.cmu.edu

Abstract: The ability to specify or control spatiotemporal chemical environments is critical for controlling diverse processes from chemical synthesis to cellular responses. When established by microfluidics methods, this chemical control has largely been limited to two dimensions and by the need for using complex approaches. The ability to create three-dimensional (3D) chemical patterns is becoming more critical as microfluidics is beginning to have novel applications at larger millifluidic scales, including model organism behavior, embryonic development, and optofluidics. Here, we present a simple approach to create 3D chemical patterns that can be controlled in space and time via two-dimensional (2D), single-layer fluidic modules. Not only can we employ autonomous flow in a 2D fluidic configuration to produce a 3D pattern, but with very simple changes in the 2D configuration, the chemical pattern can be "focused and defocused" within the 3D cross section. We also show that these chemical patterns can be predicted by computational fluid dynamics simulations with high experimental correlation. These simulations allow analyses of the characteristics of interface behaviors with respect to three basic yet critical parameters that need to be thoroughly considered in scaling-up from microfluidic to millifluidic research: Reynolds number (*Re*), inlet geometry, and channel height. The findings not only indicate proof of concept for 3D pattern creation but also reveal that a number of fluidic experiments may have inherent limitations resulting from unrecognized 3D profiles that depend on these parameter choices. These results will be useful for research areas including embryonic development, cellular stimulation, and chemical fabrication approaches.

Introduction

Spatiotemporal manipulation of three-dimensional (3D) chemical patterns requires highly integrated microdevices that have proven successful in diverse fields ranging from biological response to chemical interface applications.[1−5] Microfabrication approaches have enabled high-throughput microcomponents (e.g., sensors, mixers, valves, pumps) to be coupled together into multilayer microfluidic devices.[6] However, focusing on simple principles to generate complex responses can yield significant technological advances. Thus, rather than continuing to miniaturize and integrate many complex elements, one may derive advantages from basic principles that have been previously overlooked. A diversity of two-dimensional (2D) microfluidic studies have been published that rely on 2D visualization of the microfluidic interfaces with conventional inverted optical microscopes to characterize the chemical distributions and patterns.[7] This simple procedure may have led to a misunderstanding of real 3D chemical profiles, especially as the scale of the fluidics transitions from the micro- to the millifluidic range. These profiles can be sensitive to parameters derived from the flow conditions and channel geometries. The sensitivity of the chemical profile to these parameters becomes more critical as microfluidic applications are scaled-up to the millimeter range, which has begun to occur in a diversity of areas including studies of model organism behaviors in microfluidics,[8,9] embryonic development,[10−12] optofluidics,[13−15] and passive mixing,[16,17] even though the flow is still laminar throughout the channel.

[†] Department of Mechanical Engineering.
[‡] Department of Biomedical Engineering.
[§] Department of Biological Sciences.

(1) Burns, M. A.; Johnson, B. N.; Brahmasandra, S. N.; Handique, K.; Webster, J. R.; Krishnan, M.; Sammarco, T. S.; Man, P. M.; Jones, D.; Heldsinger, D.; Mastrangelo, C. H.; Burke, D. T. *Science* **1998**, *282*, 484–487.
(2) Thorsen, T.; Maerkl, S. J.; Quake, S. R. *Science* **2002**, *298*, 580–584.
(3) Therriault, D.; White, S. R.; Lewis, J. A. *Nat. Mater.* **2003**, *2*, 265–271.
(4) Skelley, A. M.; Kirak, O.; Suh, H.; Jaenisch, R.; Voldman, J. *Nat. Methods* **2009**, *6*, 147–152.
(5) Groisman, A.; Lobo, C.; Cho, H. J.; Campbell, J. K.; Dufour, Y. S.; Stevens, A. M.; Levchenko, A. *Nat. Methods* **2005**, *2*, 685–689.
(6) Hong, J. W.; Quake, S. R. *Nat. Biotechnol.* **2003**, *21*, 1179–1183.
(7) Atencia, J.; Beebe, D. J. *Nature* **2005**, *437*, 648–655.
(8) Chung, K. H.; Crane, M. M.; Lu, H. *Nat. Methods* **2008**, *5*, 637–643.
(9) Chronis, N.; Zimmer, M.; Bargmann, C. I. *Nat. Methods* **2007**, *4*, 727–731.
(10) Lucchetta, E. M.; Lee, J. H.; Fu, L. A.; Patel, N. H.; Ismagilov, R. F. *Nature* **2005**, *434*, 1134–1138.
(11) Dagani, G. T.; Monzo, K.; Fakhoury, J. R.; Chen, C. C.; Sisson, J. C.; Zhang, X. J. *Biomed. Microdevices* **2007**, *9*, 681–694.
(12) Raty, S.; Walters, E. M.; Davis, J.; Zeringue, H.; Beebe, D. J.; Rodriguez-Zas, S. L.; Wheeler, M. B. *Lab Chip* **2004**, *4*, 186–190.
(13) Psaltis, D.; Quake, S. R.; Yang, C. H. *Nature* **2006**, *442*, 381–386.
(14) Garnier, N.; Grigoriev, R. O.; Schatz, M. F. *Phys. Rev. Lett.* **2003**, *91*, 054501.
(15) Yang, A. H. J.; Moore, S. D.; Schmidt, B. S.; Klug, M.; Lipson, M.; Erickson, D. *Nature* **2009**, *457*, 71–75.
(16) Liu, R. H.; Stremler, M. A.; Sharp, K. V.; Olsen, M. G.; Santiago, J. G.; Adrian, R. J.; Aref, H.; Beebe, D. J. *J. Microelectromech. Syst.* **2000**, *9*, 190–197.
(17) Wang, H. Z.; Iovenitti, P.; Harvey, E.; Masood, S. *J. Micromech. Microeng.* **2003**, *13*, 801–808.

This is contrary to the recent trend of focusing on nanofluidics, which has been one main direction of research in this field. In addition to scaling differences, a very useful feature of three-lane systems where three inlets converge to a main channel is that not only can the 3D profile be controlled, but the cross-section flow profile of the center lane in such a system can be "focused and defocused" through simple approaches (e.g., defocusing from a stable 3D chemical pattern of a floating diamond surrounded by an aqueous solution). This focusing and defocusing is not a dynamic process but can be readily accomplished with different microfluidic inlet configurations; these require new fluidic channels. This 3D profile manipulation could be important in a diversity of fields such as complex 3D stimulation of cells or tissues in an embryo by controlling the profile of chemical stimulation of 3D biological systems[10,18] or flow cytometry analysis of cells and particles.[19] This pattern formation also would be useful in manipulating passive mixing in fluidic channels. This manipulation has been applied mainly to microfluidic channels with complex geometries such as serpentine shapes[16] and patterned grooves.[17] Furthermore, 3D pattern focusing and defocusing can be applied to the interaction between two immiscible fluids, where these systems have already been shown to form previously unexpected complex patterns.[20]

Conventionally, microfluidic interfaces have been characterized in terms of their 2D chemical patterns. The interfaces between aqueous fluids have been mostly considered nearly vertical and linear from the top to the bottom of the microfluidic channel, creating a step gradient across the width of the channel (which we will refer to as "planar") in the very low Reynolds number (*Re*) range, although transverse diffusive broadening can be faster in the region near the boundary walls.[21−23] Such interfaces, across which sharp chemical concentration gradients develop, have been used in a variety of biological areas including subcellular domain labeling,[18] neutrophil chemotaxis,[24] DNA−protein interactions,[25] and calcium signaling.[26] Somewhat counterintuitively though, the interfaces between co-flowing streams may deviate from being planar in scaled-up microfluidic channels and in systems that are relatively tall due to the increase in importance of the inertial force in scaled-up microfluidic channels or at relatively high Reynolds number regimes.[27] A significant number of studies have used "typical microfluidic channels" with a channel height of less than 100 μm, an average velocity of less than 10 mm/s, and a resulting Reynolds number of less than 10.[28] Upon increasing the dimensions of the channel, these planar distributions may change even though a clearly defined interface had been previously observed.[10] For example, in relatively larger systems and at a medium Reynolds number ($10 < Re < 200$) where there are nonplanar interfaces which are not centered, 3D distributions have been observed for artificial venular bifurcations[29,30] and have been analytically derived for a few cross-section geometries.[31] In this range of the Reynolds number, both viscous and inertial forces are important. As a result, the fluid flow, when multiple channels intersect, generates secondary flows (e.g., Dean flow[28]) in the channel cross section in addition to the bulk flow along the axis of the channel downstream.

While defined interfaces have been demonstrated in a variety of areas, it is likely that increasing microfluidic dimensions significantly alters idealized flow assumptions. This added complexity provokes the need and provides the opportunity to develop advanced 3D control, which we show can be simply accomplished by exploiting 2D geometries, which are already conventionally used. We can infer from previous studies[29,30] that a nonplanar interface can be created as a result of flow momentum diffentials between streams. Even noncentered interfaces that occur as a result of differing channel flow rates can produce planar irregularity, and these issues can be a challenging aspect of almost all 2D two-lane systems.[32,33] Furthermore, the developed pattern may be even more complicated when the central stream is located in a three-inlet channel where the central stream flows at a lower flow rate than those of the other outer streams, or when there is a general flow rate differential between the streams such as is employed in hydrodynamic focusing.[34] Beyond active flow control, one increasingly popular technique to precisely manipulate flow rates in microfluidics is to exploit microfluidic modules.[35−37] This modular microfluidic approach is relatively easier to implement than current microfluidic-based architectures that are multilayer and highly integrated with complex connections and components.[38] These also have advantages over single-layer, complex microfluidic systems (e.g., chemical gradient generators[24]). Here, to demonstrate our 2D approach to control 3D chemical patterns, we use simple autonomous control and simple microfluidic modules to specify fluidic channel flow rates. We accomplish 3D chemical control using basic 2D configurations of three-inlet converging channels with T-shaped (T), Y-shaped (Y), and parallel (P) inlet geometries and scale-dependent flow characteristics. These channels are the most commonly used inlet configurations in three-lane microfluidic channels. We further connect these to fluidic modules that can be autonomously regulated using equivalent resistances and arrange them into a network that allows manipulation of the microfluidic and millifluidic interfaces. We then specify basic parameters including the Reynolds number and the channel height to produce 3D patterns, including focusing and defocusing of the patterns, by simply changing input parameter values. These results, we believe, will open new avenues for microfluidic system research

(18) Helmick, L.; Antúnez de Mayolo, A.; Zhang, Y.; Cheng, C. M.; Watkins, S. C.; Wu, C.; LeDuc, P. *Nano Letters* **2008**, *8*, 1303–1308.
(19) Huh, D.; Gu, W.; Kamotani, Y.; Grotberg, J. B.; Takayama, S. *Physiol. Meas.* **2005**, *26*, R73–R98.
(20) Thorsen, T.; Roberts, R. W.; Arnold, F. H.; Quake, S. R. *Phys. Rev. Lett.* **2001**, *86*, 4163–4166.
(21) Ismagilov, R. F.; Stroock, A. D.; Kenis, P. J. A.; Whitesides, G.; Stone, H. A. *Appl. Phys. Lett.* **2000**, *76*, 2376–2378.
(22) Kamholz, A. E.; Yager, P. *Biophys. J.* **2001**, *80*, 155–160.
(23) Jimenez, J. *J. Fluid Mech.* **2005**, *535*, 245–254.
(24) Jeon, N. L.; Baskaran, H.; Dertinger, S. K. W.; Whitesides, G. M.; Van de Water, L.; Toner, M. *Nat. Biotechnol.* **2002**, *20*, 826–830.
(25) Brewer, L. R.; Bianco, P. R. *Nat. Methods* **2008**, *5*, 517–525.
(26) Kuczenski, B.; Ruder, W. C.; Messner, W. C.; Leduc, P. R. *PLoS ONE* **2009**, *4*, e4847.
(27) Di Carlo, D.; Irimia, D.; Tompkins, R. G.; Toner, M. *Proc. Natl. Acad. Sci. U.S.A.* **2007**, *104*, 18892–18897.
(28) Squires, T. M.; Quake, S. R. *Rev. Mod. Phys.* **2005**, *77*, 977–1026.
(29) Carr, R. T.; Kotha, S. L. *J. Biomech. Eng.−Trans. ASME* **1995**, *117*, 442–447.
(30) Hitt, D. L.; Lowe, M. L. *J. Biomech. Eng.−Trans. ASME* **1999**, *121*, 170–177.
(31) Hitt, D. L.; Macken, N. *J. Fluids Eng.−Trans. ASME* **2004**, *126*, 758–767.
(32) Kim, Y.; Kuczenski, B.; LeDuc, P. R.; Messner, W. C. *Lab Chip* **2009**, *9*, 2603–2609.
(33) Kuczenski, B.; LeDuc, P. R.; Messner, W. C. *Lab on a Chip* **2007**, *7*, 647–649.
(34) Wu, Z. G.; Nguyen, N. T. *Sens. Actuat. B−Chem.* **2005**, *107*, 965–974.
(35) Rhee, M.; Burns, M. A. *Lab Chip* **2008**, *8*, 1365–1373.
(36) Yuen, P. K. *Lab Chip* **2008**, *8*, 1374–1378.
(37) Sun, K.; Wang, Z. X.; Jiang, X. Y. *Lab Chip* **2008**, *8*, 1536–1543.

with dimensions of hundreds of micrometers to multiple millimeters. This work may well provide insight into a diversity of research areas and applications including chemical synthesis, material fabrication, and spatiotemporally regulated biological development.

Experimental Section

Modular microfluidic devices used represented three resistances and three chamber sizes (R10-200×50, R20-200×50, R60-200×50). For example, in the first label (R10-200×50), the resistance length of the channel is 10 mm, and the rectangular cross section is 200 μm wide and 50 μm high. The fluidic channels were configured with three inlet channels of rectangular cross sections that were 200 μm wide, 200 μm high (150 μm high for the P-channel), and 5 mm long. These inlet channels converged to form a single outlet channel of rectangular cross section that was 1.500 mm wide, 200 μm high (150 μm high for the P-channel), and 10 mm long. The reservoirs were connected to the modular microfluidic resistances using silicone tubing that had a 0.8 mm inner diameter (ABW00001, Fisher Scientific, Pittsburgh, PA). The modular resistances and the chambers were connected using polyethylene tubing of 0.76 mm inner diameter (Intramedic, 427416, Becton Dickinson and Co., Sparks, MD). The tubing sections between the modular microfluidic and millifluidic channels were approximately 200 mm long.

Microfluidic modular devices, including converging channels, were fabricated from polydimethylsiloxane (PDMS) (SYLGARD 184, Dow Corning, Midland, MI) using standard soft-lithography techniques.[39] Briefly, two-dimensional patterns of modular microfluidic channels were transferred to a high-resolution transparency. Fabrication of master templates for PDMS molds was performed by patterning desired height layers of negative SU-8 photoresist (MicroChem Corp., Newton, MA) on silicon wafers. After exposure to UV light and chemical developing, the wafers were used as the master templates to create the PDMS microchannels. Treatment of both surfaces of the PDMS channels and thin glass coverslides was with oxygen plasma.

Aqueous fluorescent beads [FluoSpheres (0.2 μm) red fluorescent (580/605), Introgen, Carlsbad, CA] were suspended in the reservoir for the central lane. Single planar images and *z*-series stacks of planar images within the microfluidic channel were collected using a confocal laser scanning head (SP5, Leica Microsystems, Bannockburn, IL) mounted on an inverted compound microscope (DMI6000, Leica Microsystems) with image acquisition software (LASAF, Leica Microsystems). Maximum projection and reslicing of *z*-series stacks and collection of intensity profiles were completed using ImageJ (v.1.38, Wayne Rasband, NIH) and MATLAB (The MathWorks, Natick, MA) software.

Numerical simulations of the flow field were made using the commercial computational fluid dynamics (CFD) solver, Fluent (ANSYS Inc., Lebanon, NH), in order to solve the nonlinear Navier−Stokes equations governing the conservation of mass and momentum within the fluid elements. Advection−diffusion equations were also solved to predict the flow field and the user-defined scalar species. The diffusion coefficients for the scalar species were specified to be 2.27×10^{-10} m^2/s, corresponding to that of water at approximately room temperature.[40] We assumed a Newtonian fluid having the properties of water at room temperature and no-slip boundary conditions on all the walls. The 3D computational domain was built using a structured hexahedral mesh with most of the cells having sides of 15 μm and four boundary layers (5−10 μm) near the walls. Mesh independence was verified by examining higher density meshes. The SIMPLE algorithm was implemented for pressure−velocity coupling, and all spatial discretizations were performed using the Second Order Upwind scheme. Flow rates were specified at the three inlets assuming the applied pressure in the experiments as shown in Figure 2a (below) and atmospheric pressure at the outlet. The convergence limit was set so that velocities converged within 0.1% and mass fractions for the central stream species reached their asymptotic values within 0.01%.

Results and Discussion

We constructed a system that could incorporate control of the fluidic interface as well as integrate modular components for dictating 3D patterns with a 2D approach. Figure 1 shows the modular microfluidic system and the 3D pattern formation. This system (Figure 1a) utilizes compressed air as the pressure source, one reservoir (C) holding a dilute suspension of fluorescent beads [FluoSpheres (0.2 μm), Introgen, Carlsbad, CA], two reservoirs (A and B) of deionized water, three types of microfluidic resistor modules for fluidic resistance, and three commonly used microfluidic channels geometries (T-, Y-, and P-inlets). In our design, the compressed gas provides a constant pressure to each of the three reservoirs (A, B, and C). Fluids from these three reservoirs pass through specified inlet fluidic resistances (R_{IA}, R_{IB}, R_{IC}) before entering the microfluidic channels. The fluid flow converges in the fluidic main channel and forms microfluidic interfaces between the central (C) stream and outer (A and B) streams. Figure 1b depicts our confocal microscopic image range, which was captured at vertical (*x*-axis) intervals of 5 μm, constructing 60 stacks totaling 300 μm in height (*x*-axis) with a cross section of 1.5 mm × 1.5 mm. We use three types of microfluidic modules to specify fluidic resistances to dictate the position of the central stream from one side to the other side of the main channel ($+y$ to $-y$). When the fluidic resistance ratio was R_{IA}:R_{IB}:R_{IC} = 5:1:24, the central stream was moved to the left ($-y$) side as shown in Figure 1c,d. Figure 1c displays a confocal microscopic image of 3D profiles showing nonplanar, parabolic interfaces in the T-channel. These were manipulated by flow rate differentials through the microfluidic resistor modules above (Supplementary Movie 2, Supporting Information). Figure 1d illustrates downstream section views of these curved microfluidic interfaces in the 3D T-channel view from the results of a CFD simulation under the same conditions ($Re \sim 25$) as the microscopic image in Figure 1c.

The ability to not only create but also alter and focus the 3D patterns is also demonstrated. The patterns are essentially inverted in some cases. The profiles at low Reynolds number (∼10) in T- and P-channels show central stream patterns aligning along the upper and lower boundaries with interfaces at the center of the *y*-axis (Figure 1e). We then focused the pattern simply by altering the Reynolds number (∼30) in the channels. The tornado-like defocused pattern of the central stream in the T-channel is focused into a floating diamond-like pattern centered around the middle of the *x*- and *y*-axes in the P-channel at the same Reynolds number (∼30). This floating diamond-like focused pattern lacks any chemical pattern at the upper and lower boundaries of the microfluidic channel ($+x$ and $-x$) versus previously where the tornado-like defocused pattern was mainly concentrated along these upper and lower boundaries. Diverse pattern alterations were investigated through CFD simulation with varying channel geometry and Reynolds number for three different channel heights of 100, 200, and 300 μm (Supplementary Figures 1−3, Supporting Information). The resulting forms are very dependent on the channel inlet geometry. The 3D patterns were drastically changed as the

(38) Shaikh, K. A.; Ryu, K. S.; Goluch, E. D.; Nam, J. M.; Liu, J. W.; Thaxton, S.; Chiesl, T. N.; Barron, A. E.; Lu, Y.; Mirkin, C. A.; Liu, C. *Proc. Natl. Acad. Sci. U.S.A.* **2005**, *102*, 9745–9750.
(39) Kim, E.; Xia, Y. N.; Whitesides, G. M. *Nature* **1995**, *376*, 581–584.

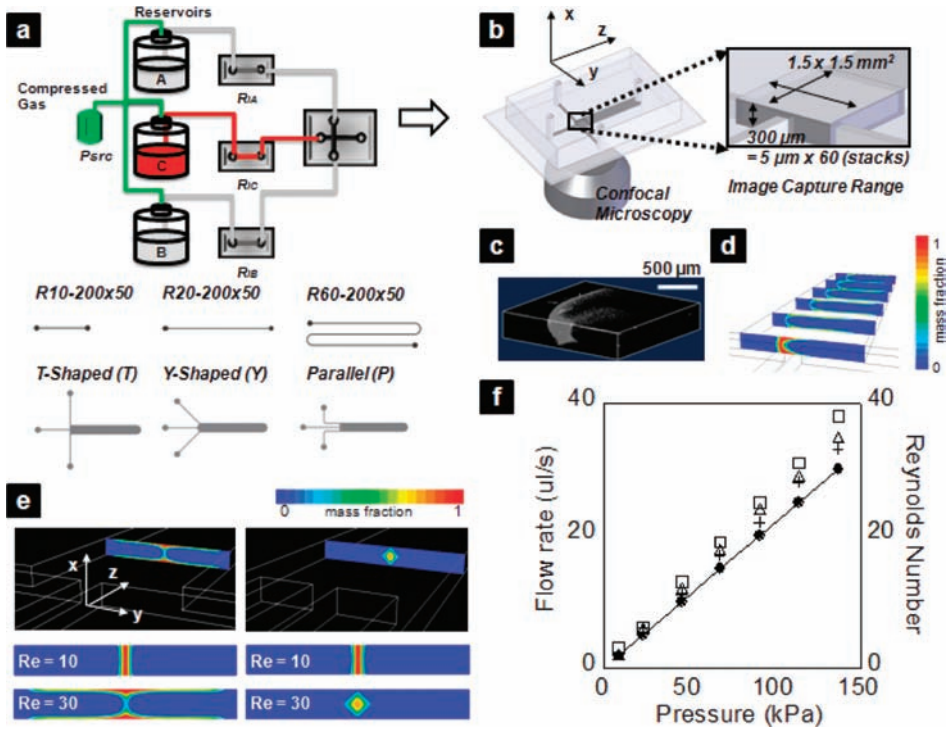

Figure 1. Controlling 3D chemical patterns with autonomous flow control and integration of 2D fluidic modules in microfluidic and millifluidic systems. (a) Schematic depicting the modular fluidic system. Compressed air provides a constant pressure (*Psrc*) to the three reservoirs from which fluids pass through specified inlet fluidic resistances (R_{IA}, R_{IB}, R_{IC}) before entering the microfluidic network. The fluid flow converges in the main channel and forms fluidic interfaces between the central stream (C) and outer streams (A and B). The three network geometries are T-shaped, Y-shaped, and P (parallel)-shaped channels with three specific fluidic resistors (R10-200×50, R20-200×50, and R60-200×50) for R_{IA}, R_{IB}, and R_{IC}. (b) Schematic showing the confocal microscopic imaging range. (c) 3D nonplanar profiles captured through confocal microscopy as shown in panel b. The scale bar is 500 μm. (d) Downstream section views from a computational fluid dynamics (CFD) simulation showing parabolic microfluidic interfaces around the central stream. The physical quantities in the legend of the panels d and e represent mass fraction from 0 (blue) to 1 (red). (e) Section views showing profile focusing and defocusing in three-inlet converging fluidic channels: T-shaped ($Re \sim 10$ in the left middle image and $Re \sim 30$ in the lower left image) and P-shaped ($Re \sim 10$ in the right middle image and $Re \sim 30$ in the lower right image) channels. (f) Flow rate and Reynolds number calculated from the pressure applied in the experiments. The circles represent the flow rate. The crosses, triangles, and squares represent the Reynolds number for channel heights of 300, 200, and 100 μm, respectively.

channel height increases at $Re \sim 15$ with very prominent focusing observed (Supplementary Figure 4, Supporting Information).

We demonstrated that these 3D patterns could be developed with a 2D microfluidic system (Figure 2). However, the 3D pattern that would be formed was not obvious. There was a direct correlation to the 3D patterns and their change with respect to the Reynolds number and the channel inlet geometry. We altered the pressure of the compressed gas and controlled the flow rates according to eq 1,

$$Q = \frac{\Delta P}{R} \tag{1}$$

where Q is the flow rate, ΔP is the pressure drop in the network, and R is the fluidic resistance at each inlet. Equation 2 shows how R relates to the channel dimensions:[41]

$$R = \frac{12\mu L}{wh^3}\left[1 - \frac{h}{w}\left(\frac{192}{\pi^5}\sum_{n=1,3,5}^{\infty}\frac{1}{n^5}\tanh\left(\frac{n\pi w}{2h}\right)\right)\right]^{-1} \tag{2}$$

where μ represents the fluid viscosity, and w, h, and L represent the channel width, height, and length, respectively.

This flow rate was used to approximate the Reynolds number using eq 3,

$$Re = \frac{\rho U D_h}{\mu} = \frac{\rho U}{\mu}\frac{2wh}{w+h} = \frac{\rho}{\mu}\frac{2Q}{w+h} \tag{3}$$

where ρ represents the fluid's density and U represents the fluid's average velocity. Figure 1f shows the flow rate and the Reynolds number, which were calculated using eqs 1−3 from the pressure applied in the experiments. The slope of the flow rate with respect to the pressure represents the reciprocal of the equivalent fluidic resistance.

Fluorescent images of the central stream and its microfluidic interface shapes are shown in Figure 2, where three schematics for the channels depict the coordinate system and patterns at specific section locations. The downstream sections ($z = 1.3$ mm) shown in the first column of these schematics were selected by considering the maximum range (1.5 mm × 1.5 mm) imaged with the 10× objective in the confocal microscope. As demonstrated in Figure 2a,g,m, the shapes of the central stream are nearly vertical and linear at $Re \sim 5$ in the T-, Y-, and P-channels (Supplementary Movies 1, 3, and 5, respectively, Supporting Information), although the 2D patterns shown in Figure 2b,h,n are different near the entrance when examining the patterns along the z-direction and are directly correlated to the inlet geometry. As shown in Figure 2d,j,p, the shapes of the central stream are no longer linear at $Re \sim 5$ in the T-, Y-,

(40) Eisenberg, D.; Kauzmann, W. *The structure and properties of water*; Oxford University Press: London, 1969.
(41) Beebe, D. J.; Mensing, G. A.; Walker, G. M. *Annu. Rev. Biomed. Eng.* **2002**, *4*, 261–286.

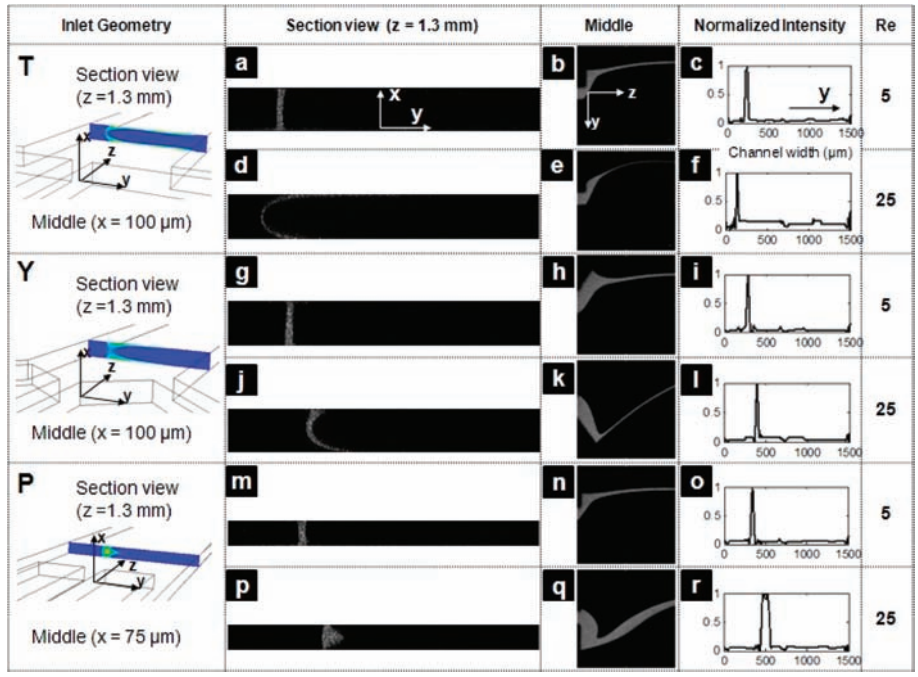

Figure 2. 2D patterns and normalized intensities of the 3D interface profiles in the T-, Y-, and P-channels. The first column in the table represents the inlet geometry shape and cross sections observed in the channels. Fluorescent images in the T-channel (a) at the downstream section $z = 1.3$ mm and (b) at the middle section $x = 100$ μm, and (c) normalized intensity in the crossing line of two planes, $z = 1.3$ mm and $x = 100$ μm, at $Re \sim 5$. For higher Re of ~25, images are (d) at the downstream section $z = 1.3$ mm and (e) at the middle section $x = 100$ μm, and (f) normalized intensity in the crossing line of two planes, $z = 1.3$ mm and $x = 100$ μm. Fluorescent images in the Y-channel (g) at the downstream section $z = 1.3$ mm and (h) at the middle section $x = 100$ μm, and (i) normalized intensity in the crossing line of two planes, $z = 1.3$ mm and $x = 100$ μm, at $Re \sim 5$. For higher Re of ~25, images are (j) at the downstream section $z = 1.3$ mm and (k) at the middle section $x = 100$ μm, and (l) normalized intensity in the crossing line of two planes, $z = 1.3$ mm and $x = 100$ μm. Fluorescent images in the P-channel (m) at the downstream section $z = 1.3$ mm and (n) at the middle section $x = 75$ μm, and (o) normalized intensity in the crossing line of two planes, $z = 1.3$ mm and $x = 75$ μm, at $Re \sim 5$. For higher Re of ~25, images are (p) at the downstream section $z = 1.3$ mm and (q) at the middle section $x = 75$ μm, and (r) normalized intensity in the crossing line of two planes, $z = 1.3$ mm and $x = 75$ μm.

and P-channels (Supplementary Movies 2, 4, and 6, respectively, Supporting Information). The pattern is curved at $Re \sim 25$ in the T-channel (Figure 2d), which is different from the vertically aligned interface pattern at the downstream position (Figure 2a). The pattern is altered at the same Reynolds number into a triangular form floating above the lower boundary wall in the P-channel (Figure 2p). These patterns are also characterized in the fourth column of normalized intensities (Figure 2) through calculating the intensity at the line where the two planes cross ($z = 1.3$ mm and middle ($x = 100$ μm (T and Y) or 75 μm (P))) for the channel shapes. For example, the central lane thickness at the middle section in the third column (Figure 2) is found to be different between the T- and P-channels (Figure 2e,q), as shown in the intensity profiles in Figure 2f,r. Furthermore, the distribution at the middle section in these nonplanar 3D patterns can be significantly different from that at the bottom view. The 2D flow patterns and their normalized intensities in the middle section and the bottom views of the T-, Y-, and P-channels help clarify how these 3D patterns form in the channels at $Re \sim 5$ and 25 (Supplementary Figure 5, Supporting Information).

The T- and Y-channels in Figure 2d,j show that the pattern becomes parabolic at $Re \sim 25$. This is very different from the vertical and nearly linear alignment at $Re \sim 5$ in Figure 2a,g. These curved shapes, which may result from the parabolic velocity profile in a pressure-driven flow, become more pronounced as the flow rate differentials increase between the outer streams (A and B in Figure 1a). While both of these patterns are parabolic forms, their distribution is not the exact same across the channel in Figure 2d,j. It is possible that the fluid momentum differentials of the flow coming from each inlet are larger in the T-channel than in the Y-channel. Also, the shapes, as shown in Figure 2e,k, are different between these two geometries. This is likely due to the longer entrance length[41] of the center lane in the Y-channel (Figure 2k), which requires this distance to reach a steady-state interface position; this is a feature that is determined by the ratio of the flow rates for the streams (A and B in Figure 1a). This disruption near the entrance is related to vortex formation, which is caused by flow separation at the entrance of the inlets. For example, in this fluidic resistance configuration, this occurs when the flow velocity increases in stream B from Figure 1a. This vortex affects the chemical pattern near the entrance of the central stream, as shown in Figure 2k, which influences the 3D patterns downstream. In contrast, the pattern in the P-channel (Figure 2p) is not curved; it has a floating triangle-like focused form. This is similar to the focused pattern of the floating diamond-like form in Figure 1e, where the middle stream was centered in the P-channel at $Re \sim 30$. Therefore, it is likely that this floating diamond-like focused form in the P-channel depends on the inlet geometry, and the specific pattern shape (e.g., triangle, square) is likely determined by relative flow rates between inlets.

After experimentally demonstrating these complex, 3D flow patterns, we further implemented a computational approach to examine the range of parameters that strongly affect the 3D flow pattern. CFD simulations were used to provide a better understanding of the flow characteristics and a qualitative description of the 3D shape of the central stream. The confocal microscopic range was indicated by the gray-colored box for the T-, Y-, and P-channels in Figure 3, panels a, f, and k,

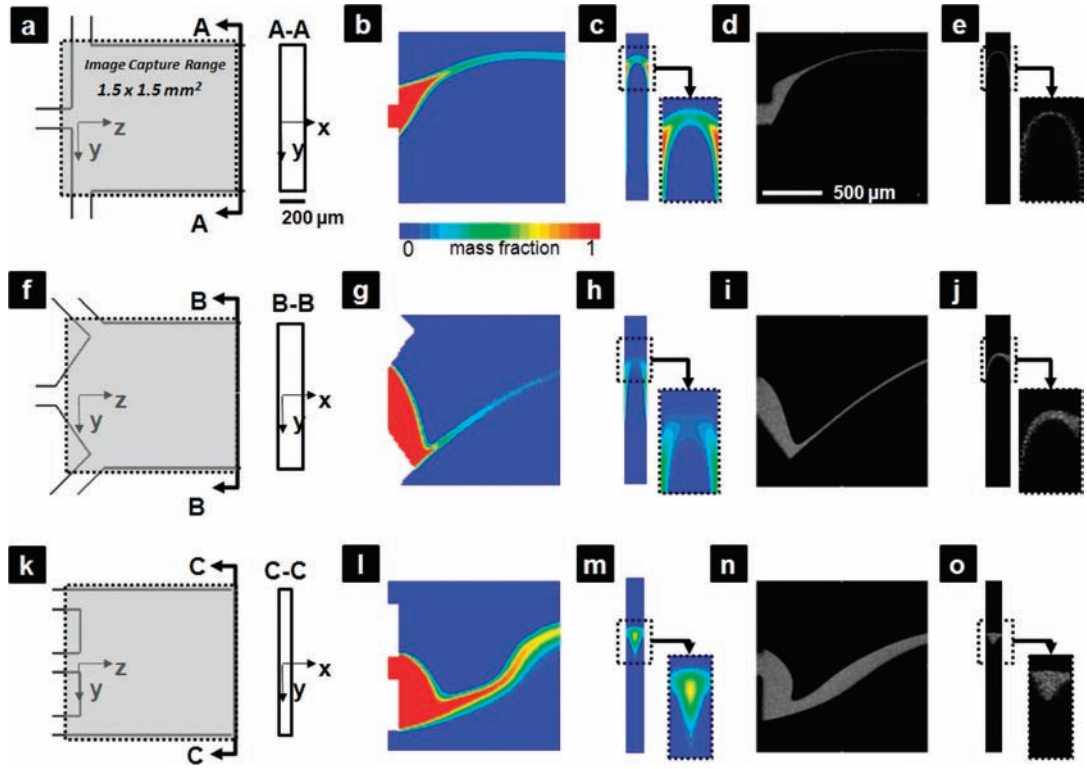

Figure 3. Experimental confocal microscopic images and CFD simulations for the T-channel, Y-channel, and P-channel. (a) Schematic depicting the image capture range and the cross-section location for the section view in the T-channel. (b,c) Section views at (b) $x = 100$ μm and (c) $z = 1.3$ mm from the simulations. (d,e) Confocal microscope section views at (d) $x = 100$ μm and (e) $z = 1.3$ mm from the experiments. (f) Schematic depicting the image capture range and the cross-section location for the section view in the Y-channel. (g,h) Section views at (g) $x = 100$ μm and (h) $z = 1.3$ mm from the simulations. (i,j) Confocal microscope section views at (i) $x = 100$ μm and (j) $z = 1.3$ mm from the experiments. (k) Schematic depicting the image capture range and the cross-section location for the section view in the P-channel. (l,m) Section views at (l) $x = 75$ μm and (m) $z = 1.3$ mm from the simulations. (n,o) Confocal microscope section views at (n) $x = 75$ μm and (o) $z = 1.3$ mm from the experiments. The physical quantities in the legend of the panels b, g, and l represent mass fraction from 0 (blue) to 1 (red).

respectively. The section views, including A-A, B-B, and C-C, show the patterns at the downstream ($z = 1.3$ mm). The simulations (Figure 3b,c) were compared with the experimental results (Figure 3d,e) under the same conditions ($Re \sim 25$) in the T-channel. Simulation results in the middle section ($x = 100$ μm, Figure 3b) and the downstream section ($z = 1.3$ mm, Figure 3c) are in good agreement with the corresponding experimental fluorescent images (Figure 3d,e). Likewise, simulation results in the Y-channel (Figure 3g,h) and P-channel (Figure 3l,m) closely corresponded to experimental results in the Y-channel (Figure 3i,j) and P-channel (Figure 3n,o). It is noted that there are some minor differences, such as the lane thickness. The central lane thickness in the simulations is a little broader than in the experimental results, yet this is likely due to the transverse diffusive dispersion being considered in the simulation based on the diffusion coefficient of water. Dispersion should be negligible in the experiments due to the size of the fluorescent beads (0.2 μm) that have little diffusion when compared to water, which explains the minor difference between the experiments and the CFD results. The diffusion coefficient of the beads (0.2 μm in diameter) used in the experiment is approximately 1.1×10^{-12} m^2/s, which is over 100 times smaller than that of water, 2.2×10^{-10} m^2/s. The beads in water solution were effectively exploited to track the central lane flow pattern in our experiments. For our modeling, we used the diffusion coefficient of water due to the use of aqueous solutions in a diversity of applications with these systems.

We further used our approach to build a quantitative assessment of important parameters, which could be used to create and control 3D patterns with 2D systems, especially at larger sizes transitioning from microfluidic to millifluidic systems. These parameters include Reynolds number, channel height, and inlet geometry. Figure 4 shows the patterns formed using a fixed height (200 μm) for the channels with varying Reynolds number and inlet geometry. The central streams are nearly vertical and planar from the top to the bottom boundaries at low Reynolds number ($\sim$5) as shown in Figure 4a(i), (v), and (viii). When the Reynolds number increases to 25, the central stream pattern becomes intensely curved at the upper and bottom walls in the T- and Y-channels [Figure 4a(iii) and (vi)] but mainly floats above the wall in the P-channel [Figure 4a(ix) and (x)]. The 2D flow patterns in the middle section (Figure 4b) and the bottom (Figure 4c) view of the channel help elucidate how these unique 3D shapes form as the Reynolds number increases. The distribution at the middle section can be significantly different from that at the bottom view. For example, for the T-channel at $Re \sim 25$, the distribution in the middle is narrow [Figure 4b(iii)], while the distribution is extremely broad with much greater curvature for the bottom view [Figure 4c(iii)]. This observation correlated well with the experimental results (Supplementary Figure 5, Supporting Information), as the pattern formation appears to be correlated to two points: (1) the vortex formation near the entrance region of the central stream and (2) the fluid momentum differentials of the parabolic velocity profile. The shape type depends on the inlet geometry (e.g., the amount of fluid momentum introduced from the side inlet channels). The significant pattern changes are even more obvious in the Y-channel as the pattern

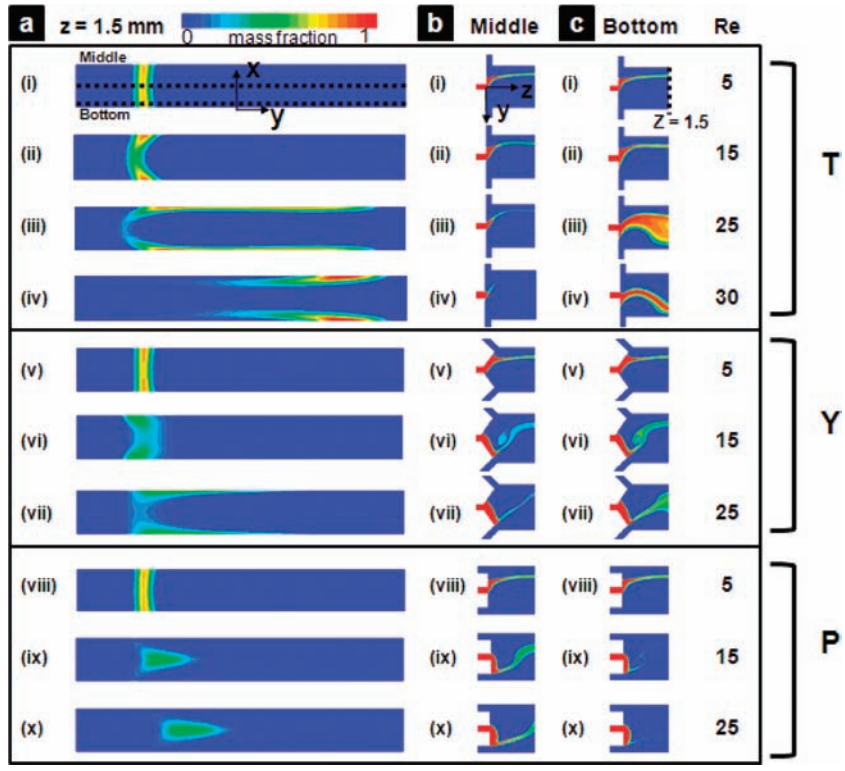

Figure 4. CFD simulations for the T-, Y-, and P-channels 200 μm high and with predefined Reynolds numbers. (a) Downstream section views at $z = 1.5$ mm in the T-channel [(i)−(iv)], the Y-channel [(v)−(vii)], and the P-channel [(viii)−(x)]. (b) Middle section views at $x = 100$ μm in the T-channel [(i)−(iv)], the Y-channel [(v)−(vii)], and the P-channel [(viii)−(x)]. (c) Bottom views at $x = 0$ μm in the T-channel [(i)−(iv)], the Y-channel [(v)−(vii)], and the P-channel [(viii)−(x)]. The physical quantities in the legend of the panels represent mass fraction from 0 (blue) to 1 (red).

appears to be partially floating at $Re \sim 15$ [Figure 4a(vi)] but curved at the walls at $Re \sim 25$ [Figure 4a(vii)]. This tremendous change occurs with only a small change in parameters within the same inlet geometry. One reason that this considerable transition occurs is the flow momentum in the Y-channel, which has characteristics of the flow in both the T- and P-channels; the Y-inlet geometry is intermediate between those of the T- and P-channels. In addition, the flow patterns shaping the vortex in the Y-channel appear similar to the patterns in the P-channel in the entrance region before the fluid flow reaches the entrance length.[42] In downstream regions, they tend to follow the patterns in the T-channel. For example, Figure 4b(vi) and 4c(vi) shows the vortex formation near the entrance region of the central stream, and Figure 4b(vii) and c(vii) shows the separation at the stream-B (from Figure 1a) entrance. When the Reynolds number reaches 30 in the T-channel (Figure 4a(iv)), the central stream and its interfaces with the outer streams no longer exist. Instead, the chemical pattern is found at the top and bottom as well as having moved to the other side, creating secondary flow from increased inertial forces of the flowing fluid. We did not observe this secondary flow in the other Y- and P-channels at the same Reynolds number, but complicated secondary flow induces complex mixing patterns at higher Reynolds number ($\sim$70).[16] We formed more 3D patterns using fixed heights (100 and 300 μm) for the channels with varying Reynolds number and inlet geometry (Supplementary Figures 6 and 7, Supporting Information). The resulting forms are very dependent on the channel inlet geometry.

On the basis of our findings, we further developed design principles that allow the control and generation of 3D patterns with simple 2D systems. This will serve as a guide for future experiments for researchers where precise 3D pattern knowledge is critical, especially at larger channel dimensions at the millimeter scale. One of the first design principles involved the channel height. Alteration of the pattern related to channel height (100, 200, and 300 μm) was explored (Figure 5a and Supplementary Figure 8, Supporting Information). At $Re \sim 15$ in Figure 5a, the shape is nearly vertical through the 100 μm height of the channel. In Figure 5a, the pattern becomes intensely curved or floating when the channel height is increased to 300 μm, even with the Reynolds number remaining at $\sim$15. This distribution though is not so obvious. Figure 5b shows that the thickness in the central profile in the higher P-channel becomes broader with increasing Reynolds number but then much thinner for the higher T-channels. This sensitivity to channel height is critical, as relatively larger microfluidic systems with dimensions of hundreds of micrometers to multiple millimeters are becoming of interest in areas including model organism behaviors in microfluidics,[8,9] embryonic development,[10–12] optofluidics,[13–15] and passive mixing.[16,17] The sensitivities of the pattern to channel height are shown in Figure 5c−e. The thickness of the chemical pattern is nearly the same over the range of channel height at relatively low Reynolds number ($\sim$5), as shown in Figure 5c, but is significantly different at $Re \sim 15$ (Figure 5d) and at $Re \sim 25$ (Figure 5e). This tendency for the resultant pattern to change is related to the specific channel inlet geometries as well. As the channel height and Reynolds number increase, the sensitivity of the 3D patterns also increases to a great extent. The resulting forms are also very dependent on the channel inlet geometry.

The need for fluidic channels with sizes that are larger than traditional microfluidic channels in the range of hundreds of

(42) Durst, F.; Ray, S.; Unsal, B.; Bayoumi, O. A. *J. Fluids Eng.−Trans. ASME* **2005**, *127*, 1154–1160.

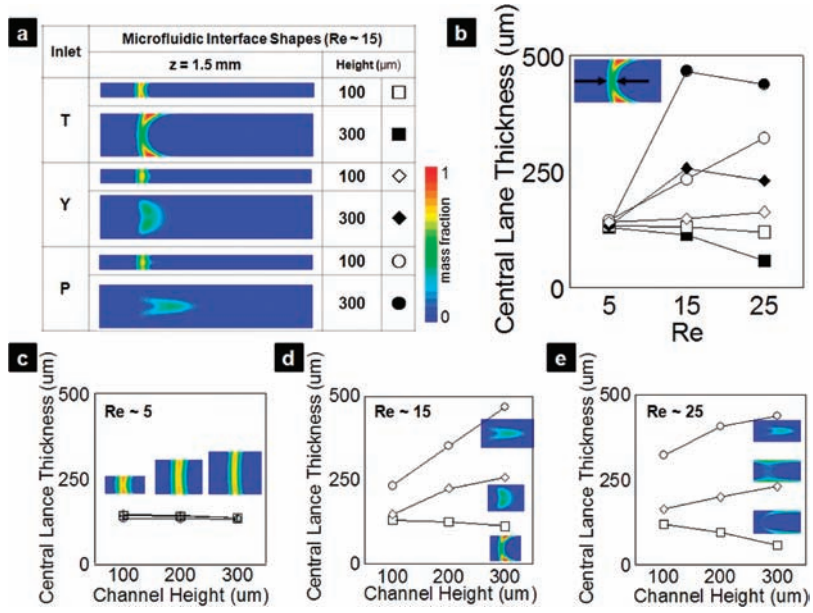

Figure 5. Microfluidic and millifluidic design considerations and sensitivity for the 3D patterns with respect to channel heights. (a) Fluidic interface shapes at the downstream section ($x = 1.5$ mm) with the channel inlet geometries (T, Y, P) and the channel height (100 and 300 μm) at $Re \sim 15$. (b) Central lane thickness over the range of Reynolds values ($5 < Re < 25$). The circles, diamonds, and squares represent the thickness in the P-, Y-, and T-channels, respectively. Filled shapes, 300 μm; open shapes, 100 μm. (c−e) Central lane thickness over the channel height at (c) $Re \sim 5$, (d) $Re \sim 15$, and (e) $Re \sim 25$. The circles, diamonds, and squares represent the thickness in the P-, Y-, and T-channels, respectively. The inset images are central stream patterns of the cross-section views at $z = 1.5$ mm for the T-, Y-, and P-channels (Figure 4 and Supplementary Figures 6−8, Supporting Information). The physical quantities in the legend of the panels represent mass fraction from 0 (blue) to 1 (red).

micrometers to single millimeters has been considered for exploring novel fields such as model organism behavior, embryonic development, multicellular stimulation, mixing layers, and chemical fabrication approaches. The sensitivity of chemical patterns to the channel height described here (Figure 5) can be applied to control and manipulate a variety of 3D profiles for these new applications without repeated fabrication and demonstration of a complicated multilayer microfluidic network.

This simple 2D approach for scaling-up fluidics using microfluidic modules and autonomous flow control is more versatile and less expensive for 3D profiles than other techniques that may or may not be able to generate these profiles. These include complex and multilayered microfluidic architectures.[2,6] Through use of 2D resistor modules (with the same cross section), control of the fluidic network can be implemented by simply calculating the flow rate and pressure relations (eq 1). They are thus independent of the main channel, which allows a tremendous amount of flexibility for frequent redesigns for various applications and experimental specifications.

To be able to have this control, the novel phenomenon in the middle range of Reynolds number ($\sim 10 < Re < \sim 30$) is exploited. The 3D profile response is important as it is outside the range for typical microfluidics showing linear and vertical fluidic interfaces [Figure 4a(i)] and for regions where passive mixing occurs due to relatively important inertial force [Figure 4a(iv)]. This middle range may have been considered to be an undefined transition zone from typical microfluidic area ($Re < \sim 10$)[28] to a chaotic mixing zone ($Re > \sim 70$)[3,16] because there may not have been any special characteristics found in this range. The relative importance though is due to the increase of inertial forces relative to viscous force. Here, we have shown that with the manipulation of the inlet geometry, this Reynolds number range can be defined in a new class to create 3D chemical patterns without chaotic mixing. Furthermore, this 3D profile is readily and precisely predictable using CFD simulations (Figure 3).

The formation of diverse 3D profiles demonstrated here (e.g., tornado-like, floating diamond, parabolic curve, etc.) is very dependent upon the channel inlet geometry. These three different channels (T, Y, and P) are the most commonly used inlet configurations in three-lane microfluidic channels. We believe other inlet shapes differing from these typical configurations will likely have distinct 3D patterns due to different flow disruption occurring near the entrance into the main channel. For example, the angle between the inlets intersecting in the main chamber determines the fluidic disruption such as separation and formation of vortices. Y-channels have shown intermediate characteristics between T- and P-channels (Figure 4b,c). Furthermore, for specific cases with these inlets, the differences are quite significant. In Figure 4a(iv), a secondary flow was predicted at $Re \sim 30$ in the T-channel due to the increasing inertial forces of the flowing fluid. This flow continues to become more chaotic as it approaches the mixing regime at $Re \sim 70$. However, this phenomenon with secondary flow did not occur in the Y- and P-channels at the same Reynolds number. A low-velocity region around the central lane entrance of these Y- and P-channels due to vortex formation is a major difference, which leads to a relatively smaller inertial momentum than in the T-channel. We thus expect that complicated secondary flow occurs at much higher Reynolds number in Y- and P-channels. This underscores the importance of the opportunities and challenges that are presented in using autonomous flow control and scaling-up micrometer to millimeter fluidic systems.

One of the challenges of scaling-up microfluidic systems (making large dimension microfluidics) is the limitation when fabricating taller channels using conventional photolithography. In addition, flow control in scaled-up microfluidic channels is challenging even though the flow is still laminar, because the bulk flow in the main channel is sensitive and is disrupted under

influences like the inlet shapes and obstacles in the flow (e.g., embryonic tissues). As the Reynolds number increases, secondary flow (e.g., Dean flow) becomes more important in the channel cross section, along with the bulk flow along the axis of the channel downstream; these may significantly affect the 3D chemical patterns. Also, as the height of the channel is increased, nonlinear 3D patterns form (Figure 5), and these may be even more sensitive, creating unexpected chemical patterns.

Conclusions

We have developed a simple 2D approach to focus and defocus 3D chemical profiles using a simple modular fluidic approach. This is applicable to fluidic systems in the transition from micrometer to millimeter scale for novel applications. We experimentally and theoretically demonstrated nonlinear 3D distribution by manipulating critical parameters: Reynolds number, inlet geometry, and channel height. The method presented here is versatile and can be applied to create and control various 3D patterns with a 2D system. Importantly, this also can serve as a guide as researchers continue to develop important fluidic applications, especially those that are larger in size than traditional microfluidics, i.e., in the range of hundreds of micrometers to multiple millimeters, and have a variety of flow conditions. We believe that these results will be very useful to researchers in the field of microfluidics and to those employing them for studies of embryonic development, chemical reactions, and optical imaging.

Acknowledgment. The authors thank Prof. Lance A. Davidson and his group members at the University of Pittsburgh for generously donating time on the confocal microscope, and Hyunjung Kim for insightful discussions on microfluidic modules. This work was supported in part by the National Science Foundation (NSF) and NSF Grant No. CMS0555513, the Beckman Young Investigators Program, the Office of Naval Research, and the Dowd-ICES Fellowship from Carnegie Mellon University.

Supporting Information Available: Supplementary movies 1−6, in .avi format, showing 3D patterns of the central lane and the microfluidic interface shapes in the T-, Y-, and P-channels at $Re \sim 25$ and $Re \sim 5$ from confocal microscopy; supplementary Figures 1−8 showing CFD simulations and confocal microscopic images. This material is available free of charge via the Internet at http://pubs.acs.org.

JA9079572